

ARTICLE

OPEN



Weakening of decadal variation of Northern Hemisphere land monsoon rainfall under global warming

Yeyan Jiang^{1,3}, Juan Li^{1,3}, Bin Wang^{1,3}, Youngmin Yang¹ and Zhiwei Zhu^{1,3}✉

Over the past century, Northern Hemisphere (NH) land monsoon rainfall (NHLMR) experienced significant decadal to multidecadal variations, mainly driven by an east–west sea surface temperature (SST) contrast over the Pacific (EWPC) and an interhemispheric North Atlantic–South Indian Ocean SST dipole (NAID). However, how the NHLMR's decadal variation would vary and whether the oceanic forcing could continue to drive it in a warming world remain unexplored. Here, by analyzing 24 Coupled Model Intercomparison Project Phase 6 (CMIP6) models' historical simulations and future projections, we show that the leading mode of decadal NHLMR will retain its nearly-uniform spatial pattern and representation of the NHLMR's intensity. In the future, the significant periodicities of decadal NHLMR are shortened as emissions levels increase. The intensity of decadal NHLMR variation will experience a comprehensive decline under various emission scenarios, which may link to the weakened intensity of NAID and EWPC. Although the relationship between EWPC and decadal NHLMR is slightly weakened in the future, EWPC will remain a primary driver while NAID is no longer. The significant historical correlation between NAID and NHLMR is mainly attributed to the influence of increased anthropogenic aerosols emission. However, the NAID-NHLMR linkage would no longer exist owing to the decline of anthropogenic aerosol emission in the future.

npj Climate and Atmospheric Science (2023)6:115; <https://doi.org/10.1038/s41612-023-00441-z>

INTRODUCTION

Monsoon is a forced response of the coupled atmosphere-land-ocean system to annual variation of solar radiation¹. Sufficient monsoon precipitation sustains nearly two-thirds of the world's population and is the source of industrial, agricultural, and domestic water. Thus, it is vital to economic and social development^{2–4}. Projecting future changes in global monsoon rainfall is of fundamental societal and scientific importance. Primary sources of the uncertainties in projecting near-term future changes of global monsoon come from the internal variability and the uncertainties in the model's representation of the real world⁵. The projected near future change of monsoons is critically affected by decadal variability. Therefore, understanding the monsoon's decadal variability and its associated physical process in a warmer climate is crucial to future climate prediction and adaptation.

Previous studies have shown that East Asian and Indian monsoon precipitation experienced decadal variability in the historical period^{6–9}. Efforts have been made to explore the causes of decadal variability in individual regional monsoons. Decadal variation of East Asian land monsoon rainfall was primarily linked to cooling over the central-eastern tropical Pacific and warming over the extratropical North Pacific and western tropical Pacific¹⁰. The interdecadal shift of the Indian summer monsoon (ISM) around the late twentieth century was attributed to Interdecadal Pacific Oscillation (IPO)¹¹. Furthermore, Atlantic Multidecadal Oscillation (AMO) and IPO also significantly contribute to the decadal variations in West Africa monsoon¹². However, on the decadal or longer time scale, monsoon rainfall is mainly regulated by planetary-scale factors¹³. Investigating monsoon decadal variability from a global perspective might be more appropriate.

Thus, by analyzing long-term observation data, the decadal variability of Northern Hemisphere land monsoon rainfall (NHLMR), which profoundly impacts the global hydroclimate, is found to be primarily driven by an east-west thermal contrast in the Pacific (EWPC) and a north-south hemispheric thermal contrast in the Atlantic and Indian Oceans (NAID)¹⁴. Both the EWPC and NAID drivers are regional manifestations of IPO/AMO related SST anomalies, which are demonstrated to modulate monsoon precipitation substantially^{15,16}.

How would NHLMR vary, and why there be such changes in the future? Progress has been made in projecting the trend and mean state of NHLMR in the warming climate^{4,17–21}. The NHLMR is projected to increase under Shared Socioeconomic Pathway (SSP) 1-2.6, SSP2-4.5, SSP3-7.0, and SSP5-8.5 using the Coupled Model Intercomparison Project Phase 6 (CMIP6) models^{22,23}. The rising temperature in the future will increase atmospheric moisture, resulting in the "wet gets wetter" pattern²⁴ if the circulation pattern remains little changed. However, future monsoons would vary considerably from region to region^{20,25}. The northern hemisphere (NH) monsoon would significantly increase compared to its southern hemisphere (SH) counterpart due to the "NH-warmer than-SH" pattern induced by greenhouse gases (GHGs) radiative forcing²⁶. Furthermore, the GHGs forcing-induced "land-warmer than-ocean" and the "El Niño-like" warming patterns will amplify the differences between northern hemispheric regional monsoons^{4,19,27}. These two essential warming patterns might particularly contribute to the different circulation changes between the South and East Asian monsoons²⁸. The fast land warming and associated Tibetan Plateau thermal forcing would strengthen the East Asian summer monsoon. In contrast, El Niño-like oceanic warming would weaken the South Asian summer

¹Key Laboratory of Meteorological Disaster, Ministry of Education (KLME)/Joint International Research Laboratory of Climate and Environment Change (ILCEC)/Collaborative Innovation Center on Forecast and Evaluation of Meteorological Disasters (CIC-FEMD), Nanjing University of Information Science and Technology, Nanjing 210044, China.

²Department of Atmospheric Sciences and International Pacific Research Center, University of Hawaii at Manoa, Honolulu, HI 96822, USA. ³These authors contributed equally: Yeyan Jiang, Juan Li. ✉email: zwz@nust.edu.cn

monsoon. However, how the NHLMR's decadal variation will change and whether the oceanic forcing will continue to drive it in a warming world remains unexplored.

In this work, based on the latest projection in the Scenario Model Intercomparison Projection²⁹ (ScenarioMIP) of CMIP6, we aim to project decadal variation of NHLMR and its linkages with oceanic drivers in the warming climate. Because the good performance of models' historical simulations is the prerequisite to a reliable projection of the future changes²⁵, we first evaluate the performance of 24 state-of-the-art models in simulating the decadal variability of NHLMR and its relationship with the two oceanic drivers. By doing so, the projection of future NHLMR is further conducted based on historical constraints. At last, the possible reason for the changes in the oceanic drivers is discussed.

RESULTS

Performance of CMIP6 models in historical simulation of decadal variations of NHLMR

Figure 1a shows the leading empirical orthogonal function (EOF) mode of observed decadal NHLMR from 1901 to 2014. Consistent with the previous studies^{14,30}, this first mode of the decadal NHLMR shows a nearly uniform spatial pattern associated with low-level southerly wind and convergence across all the land monsoon domains over NH. Since the coherent spatial feature of this mode, the NHLMR index is defined as the area-averaged of the summer mean precipitation over the entire NH land monsoon domain^{14,30}. The decadal NHLMR index is highly consistent with the principal component (PC1) of the decadal NHLMR EOF mode ($r = 0.90$, $p < 0.01$), and it represents the decadal variations of the tropical general circulation, the NH hydrological cycle, and the

decadal variations of the four sub-region (North America, Northern Africa, Indian, and East Asia) monsoon members¹⁴.

The historical simulations from the 24 models' ensemble mean (MME) (Fig. 1b), as well as almost half of the individual models (Supplementary Fig. 1), could reproduce these features realistically. To objectively quantify whether CMIP6 models can capture the uniform pattern of NHLMR, the Same Sign Rate (SSR) is employed over the domain of NHLMR (see "Method"). As shown in Table 1, compared with observation (SSR = 0.79), more than half of the models (13 of 24 models) have comparably high SSR skills (SSR ≥ 0.7). Besides the SSR, the temporal correlation coefficient between the simulated NHLMR index and the simulated PC1 of NHLMR ($TCC_{NHLMR\&PC1}$) on the decadal time scale in each model is further calculated as a criterion to evaluate whether the NHLMR index can represent NHLMR in these models. Considering both two measures (SSR ≥ 0.7 and $TCC_{NHLMR\&PC1} \geq 0.6$), nearly half of the CMIP6 models (11 of 24 models) could reproduce the decadal NHLMR reasonably.

Next, we assess to what extent the CMIP6 models could reproduce the relationship between NHLMR and its oceanic divers during the historical period. The correlation map between the NHLMR index and SSTAs (Fig. 2b and Supplementary Fig. 2) shows that the SST contrast over the Pacific is evident in nearly all 24 models. Thus, the NHLMR index is well correlated with the EWPC index, suggesting that all the models could capture the physical linkage between the NHLMR and the oceanic driver in the Pacific (Table 1). However, fewer models could reproduce the physical relation between the NHLMR and the oceanic driver of the interhemispheric SST contrast in the Atlantic and Indian Oceans (NAID), which is mainly attributable to the poor simulation in the Southern Indian Ocean (SIO) region (Fig. 2b and Supplementary Fig. 2). Most of the CMIP6 models and MME underestimated the significant negative correlations over the SIO

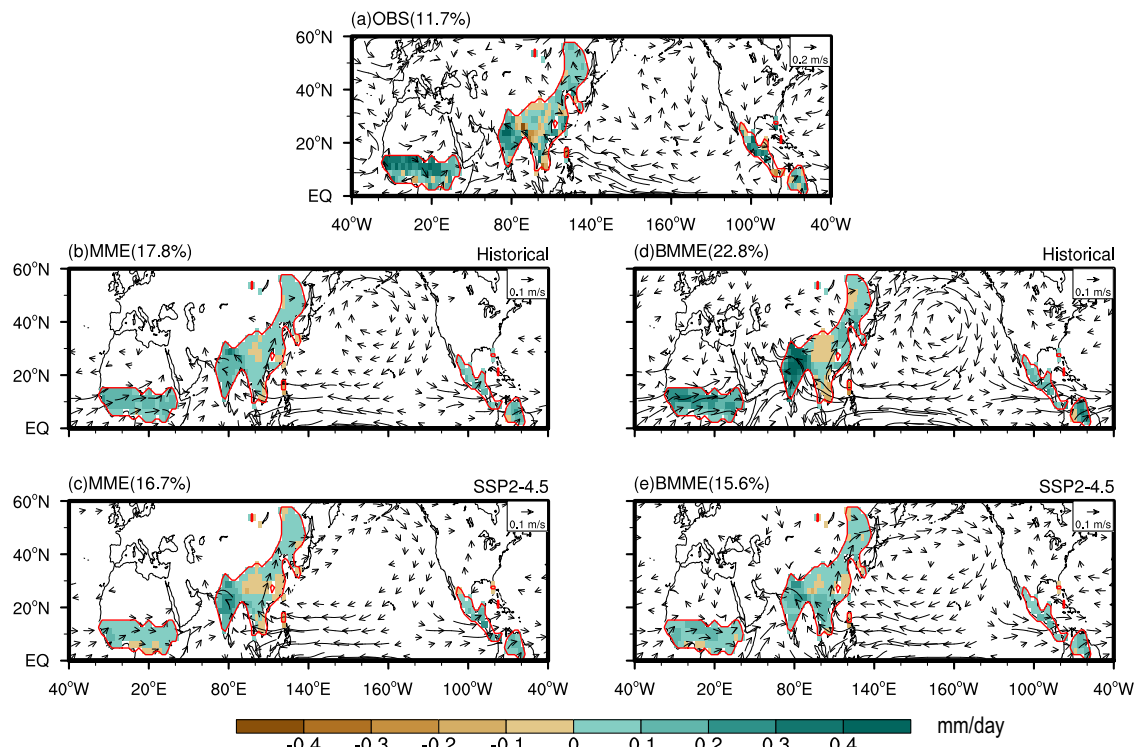


Fig. 1 The leading EOF mode of the decadal NHLMR in observation and MME/BMME. The spatial pattern of the first EOF mode of the detrended and 4-year running mean summer (MJJAS) NHLMR and its associated 850-hPa winds derived from (a) observation, MME from (b) historical simulation, as well as (c) future projections under SSP2-4.5 scenario. d, e are the same as (b, c), but for BMME. The 850-hPa wind anomalies (vectors; $m s^{-1}$) are regressed onto PC1 of NHLMR. The number on the left corner of each subfigure represents the explained variance of the EOF mode. The result of MME (BMME) is the average of the EOF modes obtained from all CMIP6 models (best six models). The NH land monsoon domains are outlined by the red contours. The period for the observation and historical simulations (future projections) is from 1901 to 2014 (2015 to 2100).

Table 1. The performance of CMIP6 models in simulating the decadal NHLMR variation and its relationship with oceanic drivers from historical experiments during the period of 1901–2014.

Model	Decadal NHLMR		NHLMR and Oceanic drivers		Three major global SST modes
	SSR	TCC (NHLMR&PC1)	TCC (NHLMR&EWPC)	TCC (NHLMR&NAID)	TCC (NHLMR& reconstructed NHLMR)
ACCESS-ESM1-5	0.83	0.87	0.60	0.13	0.49
BCC-CSM2-MR	0.49	0.10	0.51	0.56	0.67
CanESM5	0.58	0.13	0.63	0.49	0.75
CESM2	0.71	0.57	0.68	0.36	0.68
CESM2-WACCM	0.81	0.88	0.60	0.18	0.65
CNRM-CM6-1	0.68	0.22	0.47	0.31	0.63
CNRM-ESM2-1	0.53	0.27	0.28	0.42	0.45
EC-Earth3-Veg	0.74	0.51	0.49	0.48	0.51
FGOALS-g3	0.60	0.51	0.57	0.17	0.44
FIO-ESM-2-0	0.52	0.16	0.55	0.30	0.67
GFDL-CM4*	0.73	0.82	0.75	0.42	0.78
GFDL-ESM4	0.58	0.50	0.55	0.11	0.61
HadGEM3-GC31-LL*	0.80	0.89	0.50	0.48	0.80
INM-CM5-0	0.54	0.21	0.46	0.38	0.55
IPSL-CM6A-LR	0.66	0.64	0.59	0.10	0.69
KACE-1-0-G	0.77	0.84	0.53	0.24	0.49
MCM-UA-1-0	0.68	0.48	0.67	-0.04	0.78
MIROC6*	0.70	0.92	0.41	0.58	0.56
MIROC-ES2L	0.65	0.31	0.45	0.29	0.67
MPI-ESM1-2-HR*	0.84	0.91	0.64	0.45	0.74
MRI-ESM2-0*	0.73	0.63	0.58	0.35	0.61
NESM3*	0.71	0.80	0.50	0.49	0.75
NorESM2-MM*	0.79	0.95	0.80	0.48	0.83
UKESM1-0-LL*	0.72	0.77	0.55	0.68	0.76
MME	0.68	0.58	0.56	0.35	0.65
BMME	0.77	0.85	0.62	0.50	0.78
OBS	0.79	0.90	0.52	0.76	0.82

The columns from left to right represent the SSR, temporal correlation coefficient (TCC) between NHLMR index and PC1 of NHLMR, EWPC index, NAID index, and the reconstructed NHLMR index by using PCs of three major SSTAs modes in each CMIP6 model, respectively. The results with respect to the observation (OBS), the ensemble mean of all 24 models (MME), and the best six models (BMME) are also provided. The TCCs of MME (BMME) are the average of the temporal correlation coefficients obtained from the 24 individual models (best six models). The bold TCCs are significant at a 95% confidence level. The bold, asterisk and italic model names denote selected models according to their performance in simulating decadal NHLMR variability, the relationship with oceanic drivers and three major global modes, respectively.

region; some even exhibit a positive correlation. The bias is also reflected in the correlations between the NHLMR and NAID index (Table 1). Eight of 11 models that reproduce the decadal NHLMR could capture the NHLMR's linkages with EWPC and NAID index with TCCs significant at 95% level.

To further explore the underlying mechanisms responsible for the oceanic drivers of decadal NHLMR, we examine decadal modes of the observed global SST (Supplementary Figs. 3–5). The leading mode shows a zonal SST contrast over the Pacific (Supplementary Fig. 3), which bears a close similarity to the EWPC pattern (Fig. 2a). The western subtropical Pacific exhibit apparent warm SSTAs, accompanied by sharp cold SSTAs in the equatorial eastern Pacific. In addition, the principal component of this mode is highly correlated with NHLMR ($r = 0.53$, $p < 0.01$) and EWPC index ($r = 0.93$, $p < 0.01$). Thus, this SST mode is called the EWPC mode. Supplementary Fig. 3 shows that the MME and most CMIP6 models reasonably reproduce the EWPC mode over the Pacific.

The other two significant modes of global SST in observation feature a prominent warm North Atlantic (defined as the NA mode) and a cold southern Indian Ocean (defined as the SIO

mode), respectively (Supplementary Figs. 4 and 5). The NA mode resembles a warm global SST pattern with salient anomalies over North Atlantic, while the cold SSTAs are outstanding in the SIO mode. Note that the NAID index is significantly associated with both the PCs of NA and SIO modes with a correlation coefficient of 0.57 and 0.51, respectively (Supplementary Fig. 6). The two PCs can reconstruct the NAID index well with a high correlation coefficient of 0.76 (Supplementary Fig. 6). Therefore, the NA and SIO modes are the critical sources of NAID forcing. Considering this, the models' fidelity in simulating these two SST modes is measured. For the NA mode (Supplementary Fig. 4), nearly all CMIP6 models can well reproduce the warming NA SSTAs, corresponding to the good simulations in the positive NA SSTAs signals for the NHLMR (Fig. 2b). However, this is not the case when simulating the SIO mode. CMIP6 models systematically underestimated the cold SIO SSTAs (Supplementary Fig. 5), corresponding to the poor simulation of the negative SST correlation in SIO (Fig. 2b and Supplementary Fig. 2).

It is found that PCs of the first three major modes of the decadal SSTAs can well reconstruct the NHLMR index (rec-NHLMR index2,

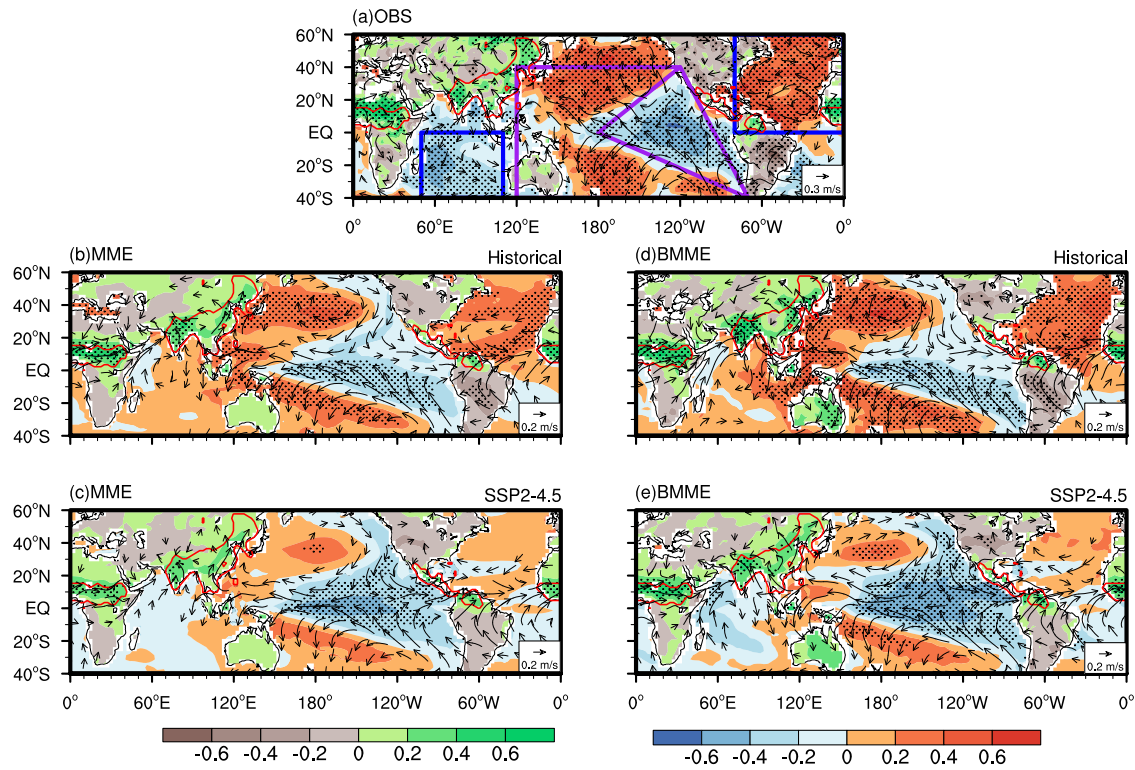


Fig. 2 SSTAs associated with the decadal NHLMR index in observation and MME/BMME. The correlation coefficients of boreal summer (MJAS) SST (shading over the ocean), land rainfall (shading over the land) and 850-hPa winds (vectors) with respect to the decadal NHLMR index in (a) observation, and MME from (b) historical simulation and (c) future projections under SSP2-4.5 scenario. d, e is the same as (b, c), but for BMME. The result of MME (BMME) is the average of the correlation maps obtained from all CMIP6 models (best six models). The NH land monsoon domains are outlined by the red contours. The blue and purple lines outline the areas used for defining the NAID and EWPC indexes. The correlation coefficients significant at a 95% confidence level by a Monte Carlo test are dotted. The period for the observation and historical simulations (future projections) is from 1901 to 2014 (2015 to 2100).

$r = 0.82$), which has a comparable capability with that by using EWPC and NAID index (rec-NHLMR index1, $r = 0.82$) in observation (Supplementary Fig. 7). The above findings further demonstrate that the first three major internal decadal modes of global SST are tightly connected to EWPC and NAID forcings and, therefore, the decadal variation of NHLMR.

How does the model simulate the decadal variation of NHLMR considering the joint effects of the three essential global SST modes? The reconstructed NHLMR index using three modeled PCs is evaluated against the simulated NHLMR index. Table 1 shows the correlation coefficients between the reconstructed and simulated NHLMR in each CMIP6 model. The best six models (i.e., GFDL-CM4, HadGEM3-GC31-LL, MPI-ESM1-2-HR, CESM2-MM, and UKESM1-0-LL) can not only well reproduce the decadal NHLMR but also nicely capture its relationship with oceanic drivers (i.e., the decadal NHLMR can be well reconstructed by the modeled three global SST major modes, with TCC larger than 0.7).

It is expected that the best six models' ensemble mean (BMME) could reasonably reproduce the dominant mode of decadal NHLMR (Fig. 1d), the correlation between NHLMR and EWPC/NAID (Fig. 2d), as well as the three major modes of global SST (Supplementary Figs. 3–5). Given the historical consistency in observation and simulation, future projection is conducted using the ensemble mean of the best six models. The ensemble mean of all 24 CMIP6 models (MME) is also analyzed for comparison.

Projected future decline of decadal NHLMR

The projections (from 2015 to 2100) of the spatial pattern of leading EOF mode of decadal NHLMR revealed from MME and BMME are in high agreement, while a slight difference exists in the

East Asian monsoon (Fig. 1c, e). Note that the explained variances show a decrement under SSP2-4.5, especially revealed by BMME. Nevertheless, the uniform pattern of the leading mode of decadal NHLMR still exists in the warming world. Therefore, it is unsurprising that the averaged rainfall over the NH land monsoon domain can well represent the leading mode of the decadal NHLMR variability in the twenty-first century (Supplementary Table 1). Although the correlation coefficients have decreased compared to the historical period, the decadal NHLMR index is still applicable to represent decadal NHLMR variation in a warming climate.

The power spectral of the NHLMR index shows that nearly all CMIP6 models can well reproduce the observed period of around 10 years but have difficulties capturing the observed period of around 20 years in the historical run (Supplementary Fig. 8a). Generally, the projected NHLMR index exhibits significant periods of around 5–20 years under the warming climate. Note that the significant periodicities are more concentrated around 10 years as the emissions level increased in the future (Supplementary Fig. 8b–d), indicating the significant periodicities are shortened under the high emissions scenario.

Figure 3a compares the changes in the intensity of decadal NHLMR under different scenarios. The intensity is measured by the standard deviation of NHLMR index. Although most CMIP6 models and MME simulated intensities are lower than the observed, the observation is within the range of the models' spread, indicating the models' ability to reproduce the observed intensity of decadal NHLMR variation. Furthermore, closer to the observation, BMME simulated a higher intensity compared to MME in historical experiments. The future intensities of decadal NHLMR from MME and BMME decrease, especially under low and medium emissions.

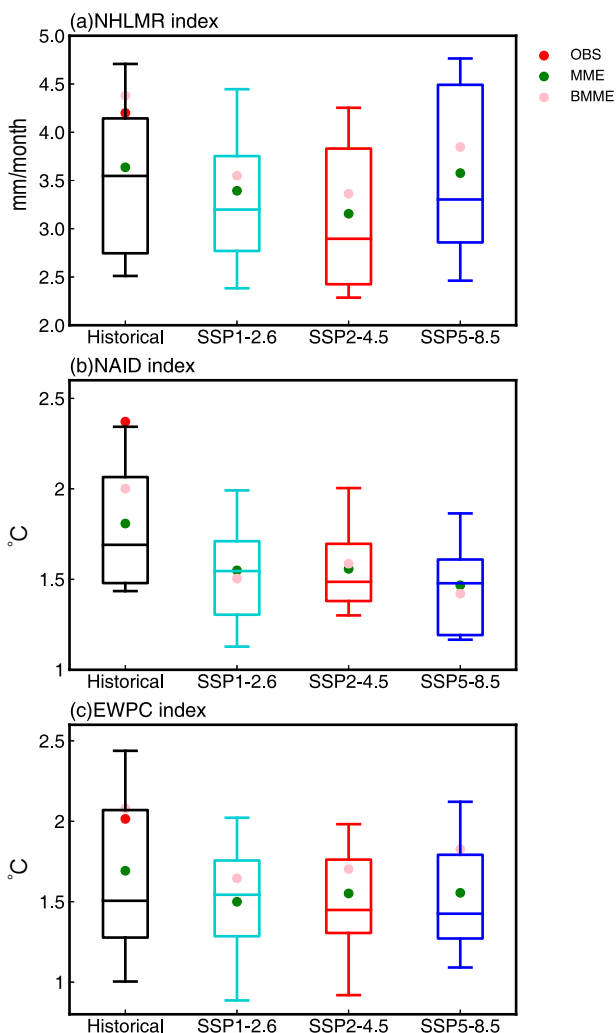


Fig. 3 The intensity of decadal variability NHLMR and two oceanic forcings in observation and CMIP6 models. The standard deviation of (a) decadal NHLMR index (units: mm month⁻¹), (b) NAID and (c) EWPC index (units: °C, the value has been multiplied by 10) in observation (red dot) and CMIP6 models from historical simulation (black box), future projections under SSP1-2.6 (aquamarine box), SSP2-4.5 (red box) as well as SSP5-8.5 (blue box) scenarios. The upper (lower) edge of the box represents the 75th (25th) range, and the vertical line segments represent the range from 5 to 95% from all CMIP6 models. The horizontal line within the box is the median. The pink and green dots represent the decadal variability obtained from BMME and MME, respectively. The intensity of MME (BMME) is the average of the standard deviations obtained from all CMIP6 models. The period for the observation and historical simulations (future projections) is from 1901 to 2014 (2015 to 2100).

Reasons for future weakening of decadal variation of NHLMR

Two possible reasons link to the future weakening of the decadal variability of NHLMR. One is the changes in the intensity of the two oceanic forcings, i.e., NAID and EWPC. Compared to observation/historical experiment, the intensity of NAID, EWPC weaken notably in future projections (Fig. 3b, c). Another is the changes in the relationship between decadal NHLMR and oceanic forcings. Thus, we check the global SSTA associated with decadal NHLMR variation in a warmer climate. Figure 2c, e displays the correlation between the decadal NHLMR index and global SST in the future. The positive correlations over the western subtropical Pacific will be slightly muted. However, the warm western subtropical Pacific and cold eastern tropical Pacific remain robust. Thus, the EWPC index is significantly related to the NHLMR index

(Supplementary Table 1), suggesting the Pacific east-west SST contrast in driving the decadal NHLMR variation will persist under a warming climate. Conversely, the north-south hemispheric SST contrast will no longer affect NHLMR in the warming scenario. The projected correlations between SIO and NHLMR will continue to be insignificant, and the positive correlation over NA will weaken in the warming world (Fig. 2), decoupling NHLMR and NAID (Supplementary Table 1). In addition to the absent correlation between NAID forcing and decadal NHLMR, correlation between EWPC and NHLMR index is also slightly reduced in the warming world (from 0.56 to 0.48 for MME, and from 0.62 to 0.57 for BMME, Supplementary Table 1).

The changes in the connection between decadal NHLMR variation and its oceanic drivers may originate from the changes in the global SST internal modes. Thus, future changes in the three major modes of global SST are examined (Supplementary Figs. 9–11). As shown in Supplementary Fig. 9, no noticeable future changes are found over Pacific for EWPC mode (Supplementary Fig. 9c, e). However, the strength of positive SSTAs over NA in the NA mode decreased remarkably (Supplementary Fig. 10c, e), contributing to the absence of linkage between NHLMR and NA in a warming world (Fig. 2c, e). Meanwhile, in comparison with the historical run, no significant changes of SIO SSTAs in SIO mode are found (Supplementary Fig. 11c, e), which is consistent with the insignificant relationship between decadal SIO SSTAs and NHLMR index (Fig. 2c, e).

In future scenarios, would the global SST major modes relate to the NHLMR-related oceanic drivers? To address this question, we calculate the correlation coefficients between PCs of each SST major mode and the NHLMR-related SSTA indices (Supplementary Table 2). The correlations between the PC of the EWPC mode and the EWPC index remain robust and even higher in the future, suggesting the more crucial role of EWPC. Meanwhile, compared with historical runs, negative correlations between the SIO index and the PC of the SIO mode remain underestimated, suggesting its role is unchanged in the warming world. Note, however, the correlation coefficients between PC of the NA mode and NA index significantly decrease in the future (from 0.73 to 0.48 for MME, and from 0.76 to 0.52 for BMME, Supplementary Table 2), corresponding to the weakening warming signal in North Atlantic under global warming as shown in Supplementary Fig. 10.

Although the relationship between the EWPC and decadal NHLMR is slightly weakened, the NHLMR decadal variability would be dominated by EWPC, while the oceanic driver of NAID would almost disappear in the warming climate, mainly due to the weakened positive SSTAs over the North Atlantic as indicated by the projected global SST major modes. Note that, we also examine the decadal variation of NHLMR and its related physical process under low and high emission scenarios (SSP1-2.6 and SSP5-8.5). The results are consistent with SSP2-4.5.

What might influence the role of the oceanic driver of decadal NHLMR variability? Why would the NAID forcing of NHLMR disappear under the warming climate? We hypothesize that the changes might be affected by greenhouse gases forcing and/or natural forcing. Besides, previous studies suggested that anthropogenic aerosol (AA) forcing profoundly influences on decadal to multidecadal changes in North Atlantic SST^{31–36} and global monsoons^{37–42}. Considering that less AA would be emitted in the future^{43,44}, the role of AA is also investigated.

Historical simulations of HadGEM3-GC31-LL during 1901–2014 are analyzed because HadGEM3-GC31-LL is the only available model that included experiments with natural forcing (hist-NAT), greenhouse gases (hist-GHG), anthropogenic aerosol (hist-AA), and all forcing (ALL) among the best six models.

It is found that the spatial patterns of the leading EOF mode of decadal NHLMR are uniform (Fig. 4a–d) with high SSR scores of 0.80, 0.67, 0.78, and 0.78 in all forcing, NAT, GHG, and AA forcing, respectively. Thus, the domain-averaged NHLMR index continues

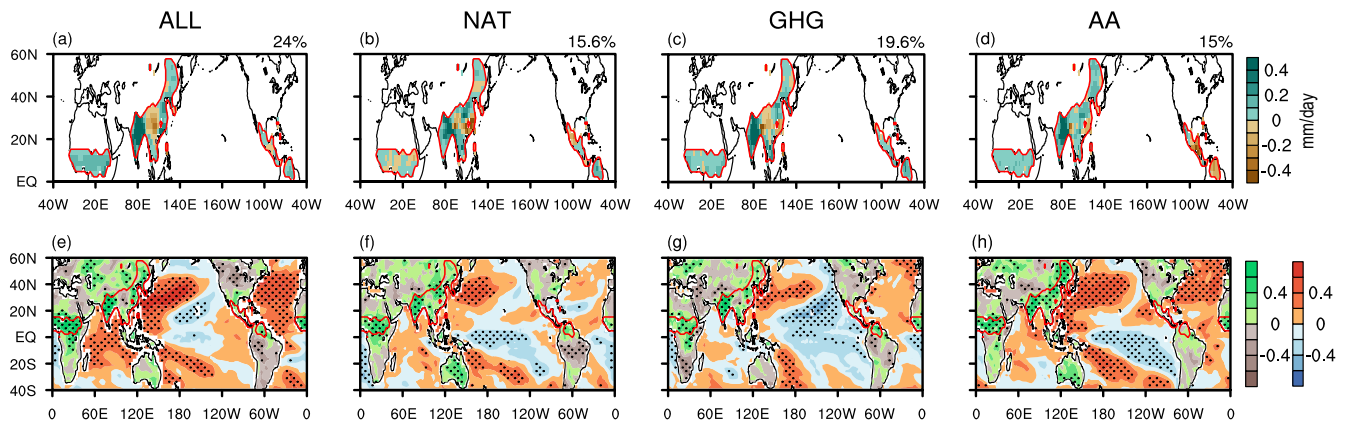


Fig. 4 The impact of external forcings on NHLMR decadal variations and its relationship with oceanic drivers during the historical period (1901–2014). Spatial patterns of the first EOF mode of decadal NHLMR from historical experiments conducted by (a) all forcing, (b) natural forcing only, (c) greenhouse gases forcing only, and (d) anthropogenic aerosols forcing only in HadGEM3-GC31-LL. e–h are the same as (a–d), but for the correlation maps of boreal summer (MJJAS) SST (shading over the ocean) and land rainfall (shading over land) with respect to the decadal NHLMR index. The correlation coefficients significant at a 95% confidence level by a Monte Carlo test (method) are dotted. The NH land monsoon domains are outlined by the red contours.

Table 2. The role of external forcings in the relationship between decadal NHLMR and its oceanic drivers during the historical period (1901–2014).

TCC	ALL	hist-NAT	hist-GHG	hist-AA
EWPC&NHLMR index	0.50*	0.31	0.50*	0.54*
NAID&NHLMR index	0.48*	0.01	0.30	0.55*

The TCCs of the decadal NHLMR index with respect to EWPC and NAID index under all forcing (ALL), and the individual forcing of natural forcing (hist-NAT), greenhouse gases (hist-GHG), and anthropogenic aerosols (hist-AA) simulations in HadGEM3-GC31-LL. The bold (asterisk) numbers represent the correlations significant at a 95% (99%) confidence level.

to represent NHLMR (Supplementary Table 3). However, relatively lower TCC can be observed in the hist-NAT simulation due to relatively large spatial heterogeneity of the leading EOF mode. The SSTAs related to the decadal NHLMR index suggest that EWPC always appears regardless of what types of external forcings (Fig. 4e–h), but significant North Atlantic warming SST anomalies only appear in the presence of AA forcing. No significant correlations exist between the North Atlantic SST and NHLMR under the NAT and GHG forcing, suggesting the importance of the AA forcing in linking the North Atlantic SST and NHLMR. Table 2 further manifests that the high correlation coefficient between the decadal NHLMR and NAID index from the all-forcing experiment is mainly due to the higher correlation under the AA forcing rather than that under the NAT or GHG forcing. These results indicate that the significant positive correlations between decadal NHLMR and NA SSTAs mainly result from the historically high emissions of AA. Thus, given the decreasing of AA emissions in the future, we infer that NA SSTAs would not be the driver of decadal NHLMR anymore. On the other hand, significant and higher TCCs between EWPC and NHLMR can be obtained in GHG and AA forcing (Table 2).

The NA SST mode under different external forcings (Supplementary Fig. 12e–h) further demonstrates that AA forcing plays a more important role in favoring warmer NA SSTAs since the highest TCC between the PC of NA mode and the NA index can be observed in AA forcing (Supplementary Table 3). In contrast, the other two global SST major modes associated with EWPC and SIO SST patterns have no significant differences among external forcings, except for the colder SIO SSTAs under NAT forcing (Supplementary Fig. 12a–d, i–l and Table 3).

DISCUSSION

In this study, we first evaluate the performance of CMIP6 models in simulating the decadal variability of NHLMR and its associated oceanic drivers in historical experiments. Different with previous studies that mainly concern models' capability in simulating monsoon precipitation variations^{45–47}, here we emphasize how model simulate the underlying ocean-atmosphere interaction processes and physical mechanisms behind monsoon variability, which is more important for model improvement. Meanwhile, a reasonable simulation in the critical physical process may allow for more reliable future projections. Thus, models' performance on five physical features related to the decadal variation of NHLMR are considered as the criteria for selecting reliable models, which consists of (1) the SSR of leading EOF pattern of decadal NHLMR, the TCC between simulated NHLMR index and simulated (2) PC1 of NHLMR, (3) EWPC index, (4) NAID index, and (5) the NHLMR index reconstructed by three SST modes. Periodicity is left out since the model's capabilities in simulating physical mechanism do not depend on whether the simulated periodicity match to the observation or not.

Using reliable models, we further investigate the decadal NHLMR variation and its associated SST drivers under a warming climate. The projections of the leading mode of decadal NHLMR variation continue to show a coherent pattern. The significant periodicities of decadal NHLMR are shortened as emissions levels increase in the future. The intensity of the decadal NHLMR index weakens under all three emission scenarios from 2015 to 2100, which may link to (1) the weakened intensity of the two oceanic forcings, i.e., NAID and EWPC and (2) the weakened relationship between the decadal NHLMR and the two oceanic forcings. Note that the second reason is not an independent one because when forcing weakens, the relationship should weaken too. Although the relationship between EWPC and decadal NHLMR is slightly weakened in the future, EWPC has a persistent impact on the decadal NHLMR variability in the warming climate. However, the NAID no longer couples with decadal NHLMR under global warming due to weakened warming SSTAs over NA.

Why will the NAID forcing of NHLMR disappear under the warming climate? By comparing all forcing and single-forcing (i.e., NAT, GHG, and AA) historical experiments, it is found that the warming NA SSTAs and their significant correlations with NHLMR are mainly due to the increased emissions of AA. So, these features would be disappeared with the decreasing of AA in the future, as revealed by SSP2-4.5 scenario. Besides, the relationship between the EWPC (SIO SSTAs) and decadal NHLMR is almost the same

among various forcings, and the corresponding EWPC (SIO) mode will have no significant differences in the warming world. Our findings highlight the important role of anthropogenic aerosols on the decadal SST variations in the North Atlantic and its connections with the decadal NHLMR, which is seldom discussed in previous studies.

This study paves a promising way and provide some implications for studying decadal variations of the global monsoon in the twenty-first century. In consideration of the physical mechanism related to decadal variation of NHLMR, the performances of BMME are closer to observation, making our conclusion more robust. The weakening decadal variation of NHLMR imply that the decadal prediction of NHLMR may be more difficult. We also reveal that models have common bias in simulating the linkage between SIO SST and decadal NHLMR, which may result in slight bias in the projection. It also hints that improving the performance in simulating SIO SST may help to the models' decadal prediction. The negative SIO SSTAs merely appear in the hist-NAT simulation (Supplementary Fig. 12j), indicating that the NAT forcing may link to such a bias in simulating SIO SSTA, but more experiments are needed to confirm this speculation in future studies.

Here we examined the impacts of external forcing on the decadal NHLMR variation in the historical experiments. Separating and quantifying the internal and external forcing of the decadal variations of NHLMR merits further investigations. The reason why the intensity of EWPC is reduced in the future projection is not discussed in this paper but deserves in-depth studies.

METHODS

Observational datasets and CMIP6 simulations

Observational monthly precipitation data is derived from the Climatic Research Unit (CRU) time series version 3.23 (TS3.23) on a $0.5^\circ \times 0.5^\circ$ grid during 1901–2014⁴⁸. Monthly SST is obtained from the arithmetic mean of two datasets: the Hadley Centre Sea Ice and Sea Surface Temperature dataset⁴⁹ (HadISST) with a horizontal resolution of $1^\circ \times 1^\circ$ and the National Oceanic and Atmospheric Administration extended reconstructed SST version 4 (ERSSTv4)⁵⁰ with $2^\circ \times 2^\circ$ resolution for 1901–2014. The monthly data of 850-hPa wind taken from the Twentieth Century Reanalysis (20CR) version 2c (V2c)⁵¹ with a resolution of $2^\circ \times 2^\circ$. To focus on the decadal-multidecadal variation, all the datasets are detrended and a 4-year running mean^{52,53} are applied. For the 4-year running mean time series, the year represents the second year of the 4-year mean period.

Monthly data output by historical simulations and projections under three Shared Socio-Economic Pathways (SSPs), i.e., SSP1-2.6, SSP2-4.5, and SSP5-8.5 scenarios from 24 CMIP6 models are used (Supplementary Table 4). We first calculate the EOF modes/correlation coefficients for individual models, then average the modes/correlation coefficients obtained from all CMIP6 models as the result of MME²⁰. By doing so, the internal variabilities remain in MME.

To investigate the effect of different external forcings on EWPC and NAID, we analyzed historical simulations forced separated by natural forcing (hist-NAT), greenhouse gases (hist-GHG), and anthropogenic aerosol (hist-AA) in HadGEM3-GC31-L1. The historical simulations are forced by both natural forcings (i.e., solar irradiance and volcanic aerosols) and anthropogenic forcings (i.e., GHGs and AAs). While the hist-GHG, hist-AA, and hist-NAT simulations are the same as the historical simulations, except that they are only forced by well-mixed GHGs, AAs, or natural forcings, respectively⁵⁴. All the data are re-gridded to $2.5^\circ \times 2.5^\circ$ grids. The period of the historical run is 1901–2014 in this study, and the future projections are examined in the period of 2015–2100.

Northern Hemisphere land monsoon rainfall

Following Wang and Ding⁵⁵, the land monsoon domain is defined as the summer-minus-winter precipitation exceeding 2 mm day^{-1} , and the summer precipitation exceeds 55% of the annual total. Local summer (winter) is defined as May to September (November to March) for the NH.

Same sign rate (SSR)

To quantify the models' performance in simulating the uniform pattern of the leading mode of decadal NHLMR, we define the same sign rate (SSR) as the number of positive precipitation anomalies grids divided by the sum grids in the entire NH land monsoon area in observation and each individual model respectively. The formula is shown as follows:

$$\text{SSR} = \frac{\text{num (positive precipitation anomalies)}}{\text{num (NH land monsoon)}}, \quad (1)$$

where "num" represents the number of grids.

EWPC and NAID index

According to Wang et al.¹⁴, the EWPC index is defined as the SSTA averaged over the western Pacific K-shaped region minus that over the eastern Pacific triangle region, as outlined in the purple line in Fig. 2a. This index indicated the east-west thermal contrast in the Pacific well. Similarly, the NAID index refers to the SSTA averaged over the North Atlantic ($0^\circ\text{--}60^\circ\text{N}$, $80^\circ\text{W}\text{--}0^\circ$, NA, which is also defined as NA index) minus that averaged over the South India Ocean ($0^\circ\text{--}40^\circ\text{S}$, $50^\circ\text{--}110^\circ\text{E}$, SIO, which is also defined as SIO index), which measures the north-south interhemispheric thermal contrast.

Monte Carlo test

To test the correlation coefficients between the time series at the decadal time scale, the Monte Carlo test⁵⁶ is employed, considering the reduced effective degree of freedom. The procedure includes the following three steps:

- Step 1: Generating two random independent normal distribution time series (for instance, the sample size is $n = 114$ for the historical period 1901–2014); then 4-year running mean time series can be obtained.
- Step 2: The correlation coefficient (CC) between these two-time series (the sample size is $n - 3$) is calculated. Repeating Steps 1 and 2 5000 times and get 5000 CCs.
- Step 3: Arrange these CCs in ascending order, and find the 95% (99%) percentile, which is the critical CC value at a 95% (99%) confidence level. Repeating the above steps 50 times to get the averaged critical value. The critical value of CC is 0.26 (0.36) for $n = 114$ at the 95% (99%) confidence level. Similarly, the critical value of CC is 0.30 (0.41) for $n = 86$ for the period of 2015 to 2100 at a 95% (99%) confidence level.

DATA AVAILABILITY

The data that support the findings of this study are freely available. CMIP6 model data are from the Earth System Grid Federation (<https://esgf-node.llnl.gov/search/cmip6/>). Observational precipitation CRU is from the University of East Anglia (<http://badc.nerc.ac.uk/data/cru/>). Observational sea surface temperature HadISST is from Met Office Hadley Centre (<https://www.metoffice.gov.uk/hadobs/hadisst/>), ERSST v4 is provided by the NOAA/ESRL PSD (<https://psl.noaa.gov/data/gridded/data.noaa.ersst.v4.html>). 20CR (V2c) dataset is provided by the U.S. Department of Energy, Office of Science Biological and Environmental Research (BER), and by the National Oceanic and Atmospheric Administration Climate Program Office (https://psl.noaa.gov/data/gridded/data.20thC_ReanV2c.html). All data needed to evaluate the conclusions in the paper are present in the paper and/or the Supplementary Materials. Additional data related to this paper may be requested from the authors.

CODE AVAILABILITY

The data in this study are analyzed with NCAR Command Language (NCL; <http://www.ncl.ucar.edu/>). The relevant codes in this work are available, upon request, from the corresponding author ZZ.

Received: 6 February 2023; Accepted: 27 July 2023;
Published online: 11 August 2023

REFERENCES

- Wang, B., Kim, H. J., Kikuchi, K. & Kitoh, A. Diagnostic metrics for evaluation of annual and diurnal cycles. *Clim. Dyn.* **37**, 941–955 (2010).
- Wang, B., Liu, J., Kim, H. J., Webster, P. J. & Yim, S. Y. Recent change of the global monsoon precipitation (1979–2008). *Clim. Dyn.* **39**, 1123–1135 (2012).
- Zhang, W., Zhou, T., Zou, L., Zhang, L. & Chen, X. Reduced exposure to extreme precipitation from 0.5 °C less warming in global land monsoon regions. *Nat. Commun.* **9**, 3153 (2018).
- Wang, B., Jin, C. & Liu, J. Understanding future change of global monsoons projected by CMIP6 models. *J. Clim.* **33**, 6471–6489 (2020).
- Zhou, T., Lu, J., Zhang, W. & Chen, Z. The sources of uncertainty in the projection of global land monsoon precipitation. *Geophys. Res. Lett.* **47**, e2020GL088415 (2020).
- Hu, Z. Z. Interdecadal variability of summer climate over East Asia and its association with 500 hPa height and global sea surface temperature. *J. Geophys. Res. Atmos.* **102**, 19403–19412 (1997).
- Kucharski, F., Molteni, F. & Yoo, J. H. SST forcing of decadal Indian monsoon rainfall variability. *Geophys. Res. Lett.* **33**, L03709 (2006).
- Zhou, T., Gong, D., Li, J. & Li, B. J. M. Z. Detecting and understanding the multi-decadal variability of the East Asian summer monsoon—recent progress and state of affairs. *Meteorol. Z.* **18**, 455–467 (2009).
- Yim, S. Y., Wang, B. & Kwon, M. Interdecadal change of the controlling mechanisms for East Asia early summer rainfall variation around the mid-1990s. *Clim. Dyn.* **42**, 1325–1333 (2014).
- Li, J. & Wang, B. Origins of the decadal predictability of East Asian land summer monsoon rainfall. *J. Clim.* **31**, 6229–6243 (2018).
- Huang, X. et al. The recent decline and recovery of Indian summer monsoon rainfall: relative roles of external forcing and internal variability. *J. Clim.* **33**, 5035–5060 (2020).
- Mohino, E., Janicot, S. & Bader, J. Sahel rainfall and decadal to multi-decadal sea surface temperature variability. *Clim. Dyn.* **37**, 419–440 (2011).
- Wang, B. et al. Northern Hemisphere summer monsoon intensified by mega-El Niño/southern oscillation and Atlantic multidecadal oscillation. *Proc. Natl Acad. Sci. USA* **110**, 5347–5352 (2013).
- Wang, B. et al. Toward predicting changes in the land monsoon rainfall a decade in advance. *J. Clim.* **31**, 2699–2714 (2018).
- Zhou, T., Yu, R., Li, H. & Wang, B. Ocean forcing to changes in global monsoon precipitation over the recent half-century. *J. Clim.* **21**, 3833–3852 (2008).
- Jiang, J. & Zhou, T. Global monsoon responses to decadal sea surface temperature variations during the twentieth century: evidence from AGCM simulations. *J. Clim.* **32**, 7675–7695 (2019).
- Christensen, J. H. et al. Climate phenomena and their relevance for future regional climate change. In: *Climate Change 2013: The Physical Science Basis. Working Group I Contribution to the Fifth Assessment Report of the Intergovernmental Panel on Climate Change* [eds Stocker, T. F. et al.]. (Cambridge University Press, 2013).
- Hsu, P. C., Li, T., Murakami, H. & Kitoh, A. Future change of the global monsoon revealed from 19 CMIP5 models. *J. Geophys. Res. Atmos.* **118**, 1247–1260 (2013).
- Endo, H., Kitoh, A. & Ueda, H. A unique feature of the Asian summer monsoon response to global warming: the role of different land-sea thermal contrast change between the lower and upper troposphere. *Sola* **14**, 57–63 (2018).
- Jin, C., Wang, B. & Liu, J. Future changes and controlling factors of the eight regional monsoons projected by CMIP6 models. *J. Clim.* **33**, 9307–9326 (2020).
- Chen, Z. et al. Observationally constrained projection of Afro-Asian monsoon precipitation. *Nat. Commun.* **13**, 2552 (2022).
- Eyring, V. et al. Overview of the Coupled model Intercomparison Project Phase 6 (CMIP6) experimental design and organization. *Geosci. Model Dev.* **9**, 1937–1958 (2016).
- Chen, Z. et al. Global land monsoon precipitation changes in CMIP6 projections. *Geophys. Res. Lett.* **47**, e2019GL086902 (2020).
- Held, I. M. & Soden, B. J. Robust responses of the hydrological cycle to global warming. *J. Clim.* **19**, 5686–5699 (2006).
- Lee, J. Y. & Wang, B. Future change of global monsoon in the CMIP5. *Clim. Dyn.* **42**, 101–119 (2012).
- Zorita, E. et al. Centennial variations of the global monsoon precipitation in the last millennium: results from ECHO-G model. *J. Clim.* **22**, 2356–2371 (2009).
- He, C., Li, T. & Zhou, W. Drier North American monsoon in contrast to Asian–African monsoon under global warming. *J. Clim.* **33**, 9801–9816 (2020).
- Li, T. et al. Distinctive South and East Asian monsoon circulation responses to global warming. *Sci. Bull.* **67**, 762–770 (2022).
- O'Neill, B. C. et al. The scenario model intercomparison project (ScenarioMIP) for CMIP6. *Geosci. Model Dev.* **9**, 3461–3482 (2016).
- Xue, J. et al. Multidecadal variation of northern hemisphere summer monsoon forced by the SST inter-hemispheric dipole. *Environ. Res. Lett.* **17**, 044033 (2022).
- Bellucci, A., Mariotti, A. & Gualdi, S. The role of forcings in the twentieth-century North Atlantic multidecadal variability: the 1940–75 North Atlantic cooling case study. *J. Clim.* **30**, 7317–7337 (2017).
- Hua, W., Dai, A., Zhou, L., Qin, M. & Chen, H. J. An externally forced decadal rainfall seesaw pattern over the Sahel and southeast Amazon. *Geophys. Res. Lett.* **46**, 923–932 (2019).
- Murphy, L. N., Bellomo, K., Cane, M. & Clement, A. The role of historical forcings in simulating the observed Atlantic multidecadal oscillation. *Geophys. Res. Lett.* **44**, 2472–2480 (2017).
- Qin, M., Dai, A. & Hua, W. Quantifying contributions of internal variability and external forcing to Atlantic multidecadal variability since 1870. *Geophys. Res. Lett.* **47**, e2020GL089504 (2020).
- Qin, M., Dai, A. & Hua, W. Aerosol-forced multidecadal variations across all ocean basins in models and observations since 1920. *Sci. Adv.* **6**, eabb0425 (2020).
- Booth, B. B., Dunstone, N. J., Halloran, P. R., Andrews, T. & Bellouin, N. Aerosols implicated as a prime driver of twentieth-century North Atlantic climate variability. *Nature* **484**, 7393 (2012).
- Cao, J. et al. Higher sensitivity of northern hemisphere monsoon to anthropogenic aerosols than greenhouse gases. *Geophys. Res. Lett.* **49**, e2022GL100270 (2022).
- Polson, D., Bollasina, M., Hegerl, G. C. & Wilcox, L. J. Decreased monsoon precipitation in the Northern Hemisphere due to anthropogenic aerosols. *Geophys. Res. Lett.* **41**, 6023–6029 (2014).
- Guo, L., Turner, A. G. & Highwood, E. J. Impacts of 20th century aerosol emissions on the South Asian monsoon in the CMIP5 models. *Atmos. Chem. Phys.* **15**, 6367–6378 (2015).
- Bollasina, M. A., Ming, Y. & Ramaswamy, V. Anthropogenic aerosols and the weakening of the South Asian summer monsoon. *Science* **334**, 6055 (2011).
- Cao, J. et al. Higher sensitivity of Northern Hemisphere monsoon to anthropogenic aerosol than greenhouse gases. *Geophys. Res. Lett.* **49**, e2022GL100270 (2022).
- Giannini, A. & Kaplan, A. The role of aerosols and greenhouse gases in Sahel drought and recovery. *Clim. Change* **152**, 449–466 (2019).
- Riahi, K. et al. The Shared Socioeconomic Pathways and their energy, land use, and greenhouse gas emissions implications: an overview. *Glob. Environ. Change* **42**, 153–168 (2017).
- Zhou, T., Ren, L. & Zhang, W. Anthropogenic influence on extreme Meiyu rainfall in 2020 and its future risk. *Sci. China Earth Sci.* **64**, 1633–1644 (2021).
- Du, Y., Wang, D., Zhu, J., Lin, Z. & Zhong, Y. Intercomparison of multiple high-resolution precipitation products over China: climatology and extremes. *Atmos. Res.* **278**, 106342 (2022).
- Jiang, Z., Li, W., Xu, J. & Li, J. Extreme precipitation indices over China in CMIP5 models. Part I: model evaluation. *J. Clim.* **28**, 8603–8619 (2015).
- Li, J., Yang, Y. M. & Wang, B. Evaluation of CESMv3 and CMIP5 Models' performance on simulation of Asian-Australian monsoon. *Atmosphere* **9**, 327 (2018).
- Harris, I. P. D. J., Jones, P. D., Osborn, T. J. & Lister, D. H. Updated high-resolution grids of monthly climatic observations—the CRU TS3.10 Dataset. *Int. J. Climatol.* **34**, 623–642 (2014).
- Rayner, N. A. et al. Global analyses of sea surface temperature, sea ice, and night marine air temperature since the late nineteenth century. *J. Geophys. Res. Atmos.* **108**, 4407 (2003).
- Huang, B. et al. Extended Reconstructed Sea Surface Temperature Version 4 (ERSST.v4). Part I: upgrades and intercomparisons. *J. Clim.* **28**, 911–930 (2015).
- Compo, G. P. et al. The Twentieth Century Reanalysis project. *Quart. J. Roy. Meteor. Soc.* **137**, 1–28 (2011).
- van Oldenborgh, G. J., Doblas-Reyes, F. J., Wouters, B. & Hazeleger, W. Decadal prediction skill in a multi-model ensemble. *Clim. Dyn.* **38**, 1263–1280 (2012).
- Goddard, L. et al. A verification framework for interannual-to-decadal predictions experiments. *Clim. Dyn.* **40**, 245–272 (2013).
- Zhou, T. et al. The dynamic and thermodynamic processes dominating the reduction of global land monsoon precipitation driven by anthropogenic aerosols emission. *Sci. China Earth Sci.* **63**, 919–933 (2020).
- Wang, B. & Ding, Q. Global monsoon: dominant mode of annual variation in the tropics. *Dyn. Atmos. Oceans* **44**, 165–183 (2008).
- Hope, A. C. A simplified Monte Carlo significance test procedure. *J. R. Stat. Soc. Ser. B Methodol.* **30**, 582–598 (1968).

ACKNOWLEDGEMENTS

This work was supported by the National Key R&D Program of China (2022YFF0801702), the National Natural Science Foundation of China (Grant No. 42088101) and the High-Performance Computing Center of Nanjing University of Information Science & Technology. We thank the World Climate Research Programme's Working Group on Coupled Modeling, which is responsible for CMIP6, and the climate modeling groups of this paper (listed in Supplementary Table 4) for producing and making available their model output (<https://esgf-node.llnl.gov/search/cmip6/>). We also acknowledge the University of East Anglia Climatic Research Unit (CRU) for providing the observational precipitation dataset: (<http://badc.nerc.ac.uk/data/cru/>), Met Office Hadley Centre for providing the observational sea surface temperature dataset (the Hadley Centre Sea Ice and Sea Surface Temperature dataset (HadISST)): (<https://www.metoffice.gov.uk/hadobs/hadisst/>), NOAA/ESRL PSD for providing the observational sea surface temperature dataset (NOAA Extended Reconstructed Sea Surface Temperature (ERSST) version 4): (<https://psl.noaa.gov/data/gridded/data.noaa.ersst.v4.html>), and NOAA PSL for providing the observational 850-hPa wind dataset (Twentieth Century Reanalysis (20CR) version 2c (V2c)): (https://psl.noaa.gov/data/gridded/data.20thC_ReanV2c.html).

AUTHOR CONTRIBUTIONS

B.W., J.L. and Z.Z. conceived the idea. Y.J. performed analyses. Y.J. and Z.Z. wrote the manuscript; J.L., B.W. and Z.Z. modify it. All authors provided critical feedback and helped shape analysis, and manuscript. Y.J. and J.L. are considered co-first authors.

COMPETING INTERESTS

The authors declare no competing interests.

ADDITIONAL INFORMATION

Supplementary information The online version contains supplementary material available at <https://doi.org/10.1038/s41612-023-00441-z>.

Correspondence and requests for materials should be addressed to Zhiwei Zhu.

Reprints and permission information is available at <http://www.nature.com/reprints>

Publisher's note Springer Nature remains neutral with regard to jurisdictional claims in published maps and institutional affiliations.



Open Access This article is licensed under a Creative Commons Attribution 4.0 International License, which permits use, sharing, adaptation, distribution and reproduction in any medium or format, as long as you give appropriate credit to the original author(s) and the source, provide a link to the Creative Commons license, and indicate if changes were made. The images or other third party material in this article are included in the article's Creative Commons license, unless indicated otherwise in a credit line to the material. If material is not included in the article's Creative Commons license and your intended use is not permitted by statutory regulation or exceeds the permitted use, you will need to obtain permission directly from the copyright holder. To view a copy of this license, visit <http://creativecommons.org/licenses/by/4.0/>.

© The Author(s) 2023